Concept Paper

Effect of Fault Extension Relevant to Unconformity on Hydrothermal Fluid Flow, Mass Transport, and Uranium Deposition

Hua Lin [1], Xu Xu [2] and Jianwen Yang [3,*

1   College of Environmental Science and Engineering, Guilin University of Technology, Guilin 541004, China; linhua5894@163.com
2   College of Material Science and Engineering, Guilin University of Technology, Guilin 541004, China; xuxu8485@163.com
3   School of the Environment, University of Windsor, Windsor, ON N9B 3P4, Canada
*   Correspondence: jianweny@uwindsor.ca; Tel.: +1-519-253-3000 (ext. 2181)

Abstract: In this study, a conceptual model is developed based on common features of typical unconformity-related uranium deposits in the Athabasca Basin, Canada. Three reactive flow modeling scenarios are designed to address the effect of fault extension on the formation of uranium deposits. Our results indicate that the location of the fault zone relevant to the unconformity is crucial to the fluid circulation in both the sandstone layer and the basement unit, the temperature distribution, the transport of aqueous components, and the uranium deposition. In particular, this research reveals that the circulating pattern of the basement brine is critical for the ore genesis. The reducing basal brine is capable of carrying aqueous uranium from depth to react with the shallow oxidizing fluid, being percolated to the basement from the overlain sandstone layer, for uranium precipitation. Scenarios 1 and 2, in which the fault zone is mainly in the basement, are in favor of focusing ore-forming hydrothermal fluids into the footwall area in the basement, leading to the formation of uranium deposits therein. Scenario 3, in which the fault zone is mainly in the sandstone layer with a limited extension below the unconformity, is unfavorable for the focusing of fluids, and hence no significant deposits can be formed, except for some minor uranium mineralization occurring in the footwall and other areas in the basement that are spatially associated with the upwelling flow zones in the sandstone layer.

Keywords: groundwater flow; mass transport; heat transport; hydrochemical modeling; uranium deposit

1. Introduction

It is estimated that over 30% of global uranium resources are from so-called unconformity-related uranium (URU) deposits, which are spatially related to an unconformity interface separating basinal formations from underlain basement rocks [1–3]. The regional unconformity lies at the bottom of Proterozoic conglomerate and sandstone, overlying Archean to Paleoproterozoic metamorphosed basement rocks, and intersects reactivated fault zones. Palaeoregolith usually exists around the unconformity [4,5]. The Athabasca Basin in Canada and the Northern Territory in Australia host many giant deposits of this type [6].

The Athabasca Basin is located in northern Saskatchewan and Alberta, Canada, and contains the world's largest and highest-grade URU deposits, covering an area of about 100,000 square kilometers [5]. The basement consists of Archean to Paleoproterozoic rocks that were metamorphosed during the Trans-Hudson orogeny (1800 Ma). The basin fill, known as the Athabasca Group, began to deposit around 1750 Ma and continued until around 1500 Ma [7,8]. The Athabasca Group is made up of four main sequences (from the bottom to the top): the Manitou Falls and Fair Point formations (consisting of conglomerate and sandstone); the Lazenby Lake and Wolverine Point formations (consisting of sandstone, siltstone, and mudstone); the Douglas Formation (shale); and the Carswell Formation (stromatolitic carbonates) [5]. Studies of fluid inclusions and diagenetic clay assemblages [9,10]

reveal a maximum total thickness of the sedimentary rocks of 5–7 km, although the current thickness of the Athabasca Group in the central basin is about 1.5 km due to erosion [5,7]. Fluid inclusion analysis of quartz reveals a homogenization temperature of 150 to 170 °C and a salinity of 25 wt% NaCl equivalent for the basinal brines. U/Pb dating of uraninite and Ar/Ar dating of syn-ore illite indicate that the main uranium mineralization occurred at 1600 Ma [11–13]. Most of the known URU deposits in the Athabasca Basin are located in the eastern part of the basin, and some deposits are located in the western part of the basin and other areas [5,7].

Large-scale fluid circulation and heat transport are thought to be responsible for the transport and deposition of uranium in the Athabasca Basin [4,9,14]. Uranium precipitation occurred when the oxidizing basinal fluid encountered the reducing basal brine near the sandstone-basement unconformity, and it was structurally controlled by reverse basement faults that were enriched in graphite [5,8,9]. The faulted graphite zones contributed the reducing agent (i.e., methane) for the precipitation of uraninite and also concentrated mineralized fluids to deposition sites [5,14–18]. These reverse faults are the result of brittle reactivation of older Syn-Hudsonian to late-Hudsonian structures in the Athabasca Basin [5]. Corresponding to different local tectonic settings, the width of the fault zones varies from tens to hundreds of meters, e.g., [5,19], and the dip angle varies from extremely low to nearly vertical, e.g., [14,20–22]. They occur in the basement but often extend across the unconformity into the sandstone to a different extent [13,23], ranging from tens to several hundred meters [24,25]. The deepest extension of the reverse faults below the unconformity is reported to be about 400 m, although longer and shorter variants are possible [5]. Brittle fault zones may act as conduits or barriers to enhance or impede fluid flow [26]. However, geological evidence from the Athabasca Basin [5,11,16] indicates that the fault zones of this type were reactivated after filling the basin and remained conductive until recent times, which supports the concept of the faults as conduits for ore-forming fluids.

Extensive numerical modeling has been conducted to study ore-forming hydrothermal fluid flow and its controlling factors in association with the URU ore genesis in the Athabasca Basin. For instance, Cui et al. [27] indicated that basement-hosted ore bodies tend to be formed corresponding to extensional deformation, while sandstone-hosted deposits correspond to compressive deformation. They also confirmed that buoyancy-driven thermohaline convection can penetrate over 1 km deep in the basement [28]. Pek and Malkovsky [29] linked the fluid circulation in the sandstone layer with the heat convection in the underlain basement. Li et al. [24] demonstrated the importance of the number, spacing, and orientation of basement faults in the formation of URU deposits. More recently, Eldursi et al. [25] conducted 2D and 3D numerical modeling in relation to the Cigar Lake deposit in the Athabasca Basin. However, these numerical studies have only considered the physical aspects of fluid flow and heat transport.

On the other hand, numerical studies that couple fluid flow with chemical reactions related to the URU deposits are relatively limited. Raffensperger and Garven [30] presented the first reactive mass transport modeling under equilibrium conditions with methane as a reducing agent. Aghbelagh and Yang [31] addressed the role of a faulted graphite zone by employing a kinetic approach for the dissolution and precipitation of minerals. More recently, they examined the effect of fault dip angles and permeabilities on uranium mineralization [32]. In the study by [30], the fault is restricted to the basement, whereas in those by Aghbelagh and Yang [31,32], the fault has the same and fixed extension both below and above the unconformity. Thus, previous numerical studies ignored the variation in fault extension (ranging from tens to several hundred meters) relative to the unconformity. To fill the knowledge gap, in this study, we conduct a numerical investigation into the role of different fault extensions in controlling uranium ore genesis.

Similar to previous studies [30–32], aqueous methane $CH_4^0(aq)$ is assumed to be the reductant for reducing uraninite via the following reaction (1):

$$UO_2^{2+} + \frac{3}{4}H_2O + \frac{1}{4}CH_4^0(aq) \leftrightarrow UO_2 + \frac{1}{4}HCO_3^- + \frac{9}{4}H^+, \tag{1}$$
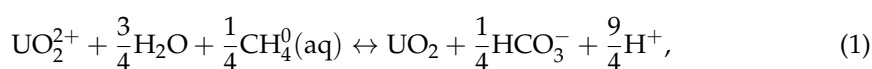
and it is produced by the reaction of graphite with water at temperatures typical of ore-forming brines as follows:

$$C + \frac{3}{2}H_2O \leftrightarrow \frac{1}{2}H^+ + \frac{1}{2}HCO_3^- + \frac{1}{2}CH_4^0(aq). \tag{2}$$
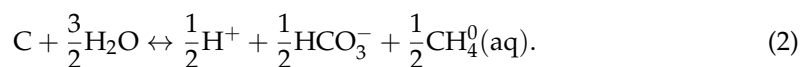
## 2. Model Development and Numerical Method

Our conceptual model does not represent any specific URU deposits in the Athabasca Basin, but it is developed by integrating some common features of typical deposits of this type in the basin. The model is characterized by a layered structure, containing a 1 km thick confining cover, a 2 km thick intermediate sandstone layer, and a 2 km thick basement unit, with the unconformity interface separating the sandstone and basement units. Previous numerical studies also employed similar layered models, e.g., [24,27,31,32]. The model has a vertical dimension of 5 km and a horizontal dimension of 6 km, and it is discretized uniformly by 160 cells both vertically and horizontally. The top boundary is 3 km below the surface. A faulted graphite zone dips to the right at an angle of 40°, having a vertical extension of 625 m (20-cell high in the vertical direction) and a thickness of 96 m (4-cell wide in the horizontal direction), which is based on a variety of research publications in relation to the fault zones in the Athabasca Basin, e.g., [14,19,21–25]. In order to simulate various fault extensions relevant to the unconformity, this study considers three scenarios, as illustrated in Figure 1. In Scenario 1 (Figure 1a), the fault zone occurs predominantly in the basement unit with an extension of 93.75 m above the unconformity. In Scenario 2 (Figure 1b), the fault zone straddles the unconformity with an extension of 250 and 375 m above and below the unconformity, respectively. In Scenario 3 (Figure 1c), the fault zone is mainly in the sandstone layer with an extension of 62.5 m below the unconformity.

The confining cover represents less permeable shallow marine sedimentary rocks, the intermediate sandstone layer is a major aquifer for fluid circulation, and the basement unit is almost impermeable. The fault zone serves as a fluid conduit as stated above. Compiled from the parameters previously employed in relevant modeling studies [24,25,27,31,32], Table 1 shows the key physical parameters of the four units, including permeability, porosity, density, and thermal conductivity, whereas Tables 2–5 tabulate the initial volume fractions of the minerals present in each unit. As brine flows through rock formations, mineral precipitation and dissolution can result in the change in porosity and permeability. In this study, this change is considered by using the commercial software package TOUGHREACT, in which the change in permeability of the rock formation is calculated from the change in porosity using ratios of permeabilities calculated from the Carman–Kozeny relationship [33,34].

The confining cover and the sandstone layer are assumed to be in oxidizing and acidic conditions, with $\log fO_2 = -14.8$ and Ph = 5.3, and $\log fO_2 = -22.8$ and pH = 5.1, respectively, where fO_2 is oxygen fugacity. The basement unit and the lower part of the faulted graphite zone in the basement are assumed to be in reducing and more acidic conditions, with $\log fO_2 = -46.8$ and pH = 4.5, and $\log fO_2 = -51.3$ and pH = 4.1, respectively. The upper part of the graphite zone in the sandstone layer is assigned the same oxidizing condition as the sandstone layer. Similar conditions were also used in previous studies [30–32].

Richard et al. [35,36] conducted fluid inclusion analysis of quartz veins in barren samples contemporaneous with major ore deposition from several uranium deposits in the Athabasca Basin, indicating that the aqueous uranium UO_2^{2+} in the basal brines has a concentration of 1.0×10^{-6} to 2.8×10^{-3} mol/L with an average of 1.0×10^{-4} mol/L. More recent fluid inclusion analysis [37] of the barren sandstone in the Athabasca Basin indicates that the concentration of UO_2^{2+} ranges from 2.2×10^{-6} to 9.9×10^{-5} mol/L with an average of 2.5×10^{-5} mol/L. Thus, in this study, UO_2^{2+} concentration is assigned to be 1.0×10^{-4} and 2.5×10^{-5} mol/L for the basement unit and the sandstone layer, respectively. In addition, it is assumed to be 1.0×10^{-6} and 1.6×10^{-6} mol/L for the confining cover and the fault zone, respectively. The initial concentrations of other aqueous components for different rock units are tabulated in Table 6, which is based on previous modeling

research [30–32]. The initial temperature distribution is calculated using a geothermal gradient of 30 °C/km, and the initial fluid pressure is determined on the basis of hydrostatic conditions.
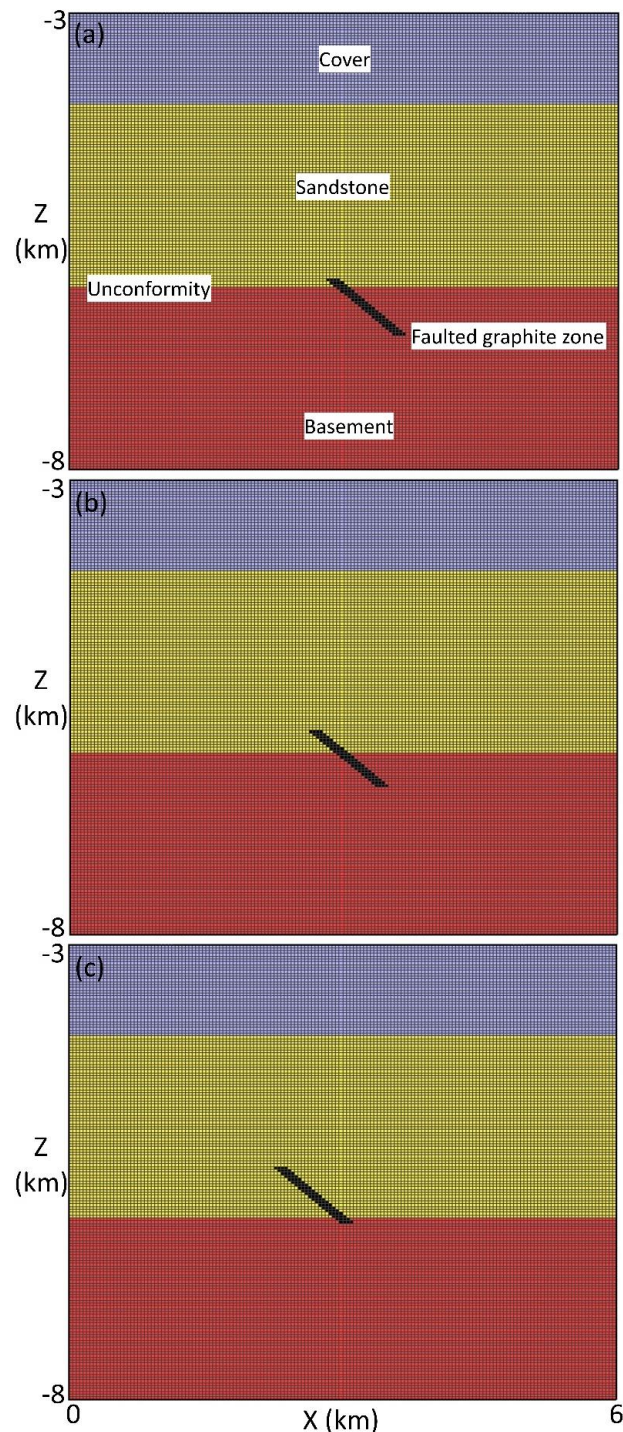
Figure 1. Conceptual model showing different hydrostratigraphic units and scenarios: (**a**) Scenario 1 with the fault zone mainly in the basement unit, (**b**) Scenario 2 with the fault zone straddling the unconformity, and (**c**) Scenario 3 with the fault zone mainly in the sandstone layer. The top and bottom are set at a constant temperature of 90 °C and 240 °C, respectively. The bottom and side boundaries are assumed impermeable, but the top is set at a fixed fluid pressure of 30 MPa. The top and bottom have fixed mineral volume fractions and aqueous component concentrations, equal to those of their respective units. For the side boundaries, the normal gradients of the volume fractions and concentrations are set to zero.

Table 1. Key physical parameters of different rock units.

Parameter	Confining Cover	Sandstone Layer	Basement Unit	Faulted Graphite Zone
Permeability (m^2)	1.0×10^{-15}	3.0×10^{-13}	3.0×10^{-16}	1.0×10^{-12}
Porosity	0.15	0.2	0.1	0.2
Density (kg/m^3)	2400	2500	2650	2400
Thermal conductivity (W/(m·°C))	2.5	3.5	2.5	4.0

Table 2. Initial mineral volume fractions of the confining cover.

Minerals	Volume Fraction
Calcite	0.44
Dolomite	0.013
Hematite	0.0003
Anhydrite	0.002
Kaolinite	0.3
Muscovite	0.001
Quartz	0.095

Table 3. Initial mineral volume fractions of the sandstone layer.

Minerals	Volume Fraction
Hematite	0.01
Anhydrite	0.006
K-feldspar	0.01
Chlorite	0.0003
Muscovite	0.02
Quartz	0.75

Table 4. Initial mineral volume fractions of the basement unit.

Minerals	Volume Fraction
Anhydrite	0.003
Chlorite	0.006
Hematite	0.0005
K-feldspar	0.05
Muscovite	0.33
Pyrite	0.0001
Quartz	0.51

Table 5. Initial mineral volume fractions of the faulted graphite zone.

Minerals	Volume Fraction
Graphite	0.085
Chlorite	0.001
Kaolinite	0.0007
Muscovite	0.42
Pyrite	0.001
Quartz	0.29

The top and bottom boundaries are set at a constant temperature of 90 °C and 240 °C, respectively. The bottom and side boundaries are assumed impermeable, but the top is set at a fixed fluid pressure of 30 MPa [27]. As for the boundary conditions of the chemical domain, the bottom and top are assumed to have fixed mineral volume fractions and aqueous component concentrations, equal to those of their respective units. For the side boundaries, the normal gradients of the volume fractions and concentrations are set to zero.

Table 6. Initial aqueous component concentrations (mol/L) of different rock units.

	AlO_2^-	Ca^{2+}	CH_4^0 (aq)	Cl^-	Fe^{2+}	HCO_3^-	K^+	Mg^{2+}	Na^+	SiO_2 (aq)	SO_4^{2-}
Cover	0.1	2.8×10^{-2}	0.1	0.1	7.3×10^{-15}	0.4	0.022	0.0026	0.1	1.0	1.5×10^{-2}
Sandstone	0.1	1.5	1.0	5.0	2.6×10^{-11}	1.0×10^{-4}	0.045	0.48	1.0	5.0	1.5×10^{-3}
Basement	0.1	0.85	1.0	2.7	0.002	0.05	0.16	0.37	0.1	1.0	5.6×10^{-4}
Fault zone	0.1	0.1	4.0	3.0	0.0005	1.2×10^{-4}	0.038	0.88	1.0	0.5	1.0×10^{-3}

Numerical simulation in this study is conducted using the software package TOUGHRE-ACT [34], which is a finite element code capable of modeling fluid flow, heat transfer, and reactive mass transport in porous media. Mineral precipitation and dissolution are assumed to be under kinetic conditions, except for anhydrite and calcite, where an equilibrium approach is employed due to their rapid reaction rate when reacting with aqueous species [34]. Further details of the numerical modeling methodology and the geochemical system can be found in the previous publications by Xu et al. [34] and Aghbelagh and Yang [31,32].

## 3. Results and Discussions

3.1. Scenario 1

Figure 2a illustrates the fluid flow vectors at 10,000 years, which is driven by buoyancy force resulting from the thermal gradient in the solution domain. Four convection cells establish in the sandstone layer with a max flow rate of 1.56 m/year. The max fluid rate in the basement is 1.24×10^{-3} m/year, three orders less than that in the sandstone. Figure 2b shows an enlarged view of the fluid flow surrounding the fault zone, indicating that the left lower half of the fault zone carries a down-flow, while the right upper half carries an up-flow. Flow vectors in the cover and basement unit are too small to be identified. To better visualize the flow pattern, the original flow vectors in Figure 2a are sparsely sampled and artificially adjusted in their length, as illustrated in Figure 2c. It can be seen from Figure 2c that the convection cells have similar size, with a dominant upwelling flow zone in the center and flanked by two downwelling zones. The other two upwelling zones, relatively narrow and weak, are close to the side boundaries. Part of the basinal fluid from the downwelling flow zones percolates across the unconformity to mix with the basement brine, which also moves downwards but at a much lower rate. The basement brine then diverges and flows upwards to join the upwelling zones in the sandstone layer. Similarly, some of the basinal fluid from the upwelling zones penetrates across the sandstone-cover interface to mix with the fluid in the cover, which also moves upwards but at a lower rate. The fluid in the cover then diverges and flows downwards to join the downwelling flow zones in the sandstone layer.

Figure 3a shows the flow vectors at 50,000 years. Two dominant convection cells now establish in the sandstone layer, with two minor cells formed close to the side boundaries. The basinal fluid circulates upwards from the top of the fault zone. When the fluid reaches the top of the sandstone layer, part of it discharges to the overlain confining cover, and the rest diverges to the left and right, and then flows downwards through the two downwelling zones that are located close to the left and right boundaries. When the fluid descends to the bottom of the sandstone layer, some of it percolates into the underlain basement, and the rest flows parallel to the unconformity interface. It is also noticed that the majority of the fluid from the left-side downwelling zone migrates horizontally towards the central part, and then merges the central upwelling zone. A small amount of it penetrates into the basement through the left lower half of the fault zone, whereas the basement brine ascends into the sandstone layer through the right upper half of the fault zone to join the central upwelling flow zone. On the other hand, the majority of the basinal fluid from the right-side downwelling zone also moves horizontally above the unconformity interface until joining the central upwelling flow. Compared with Figure 2c, now, almost all the basal brine of the entire basement is focused into the footwall area of the fault zone beneath the unconformity, except that some shallow basement brine, that is close to the side

boundaries, discharges to the sandstone layer. The fluid flow system starts to reach a steady state at about 150,000 years. Figure 3b shows the flow vectors at 300,000 years, which is similar to Figure 3a, except that even more basement brine is focused into the footwall area with fewer discharges to the overlain sandstone layer. The convective heat transport due to the afore-mentioned fluid circulation modifies the initially assigned geothermal field, leading to the temperature distribution at 300,000 years, as illustrated in Figure 3c. The mushroom-shaped isothermal line of 145 °C is resulting from the central upwelling flow and the side downwelling flow in the sandstone layer. The effect of the basement brine on the temperature distribution is negligible, as evidenced by the almost uniformly spaced isothermal lines in the basement. However, the basement flow has important implications for uranium mineralization, as follows.
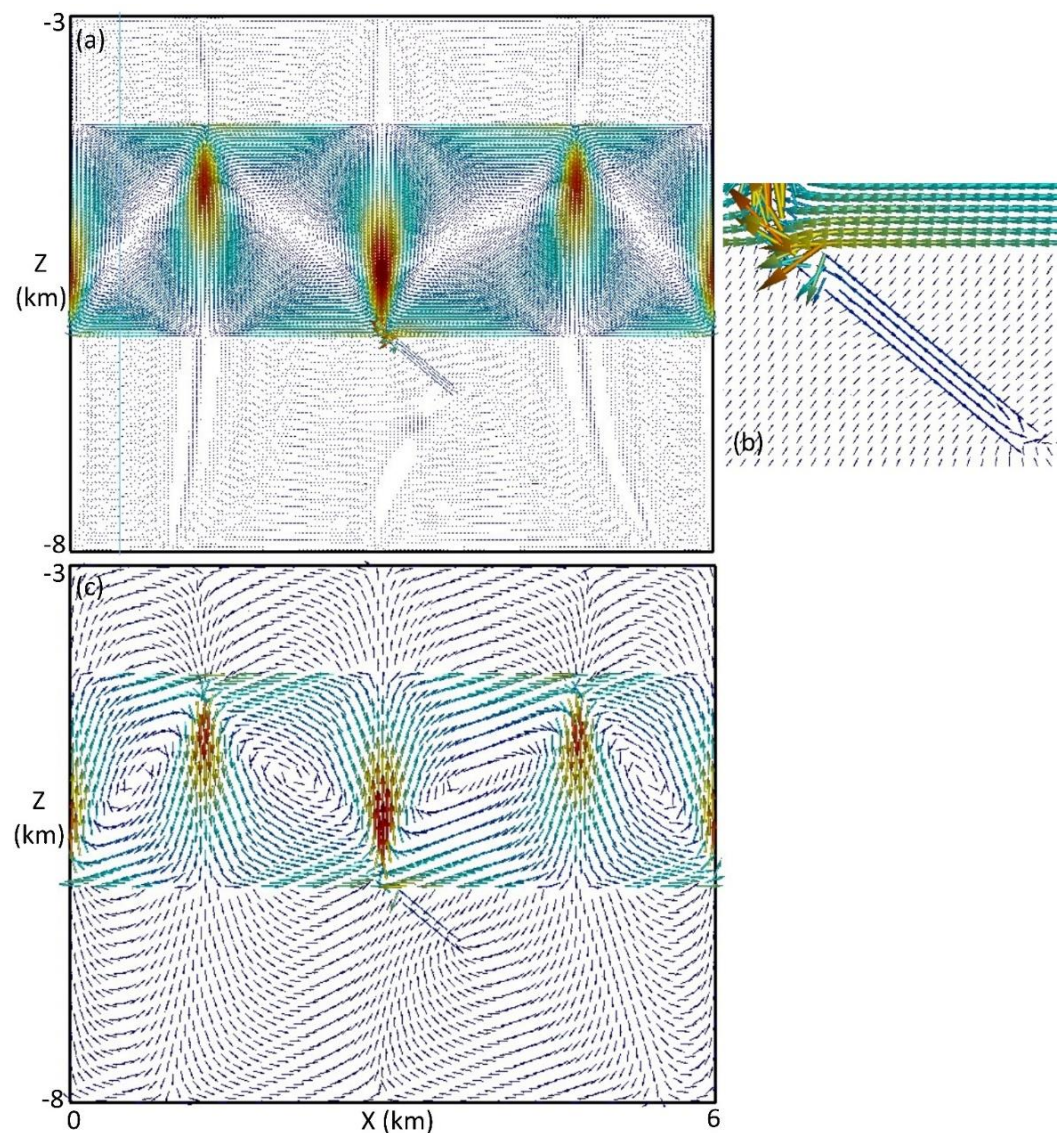
Figure 2. Numerical results of the fluid flow vectors at 10,000 years for Scenario 1: (**a**) the original flow vectors, (**b**) the enlarged view of the flow vectors surrounding the fault zone, and (**c**) the flow vectors that are sparsely sampled and artificially adjusted in length.
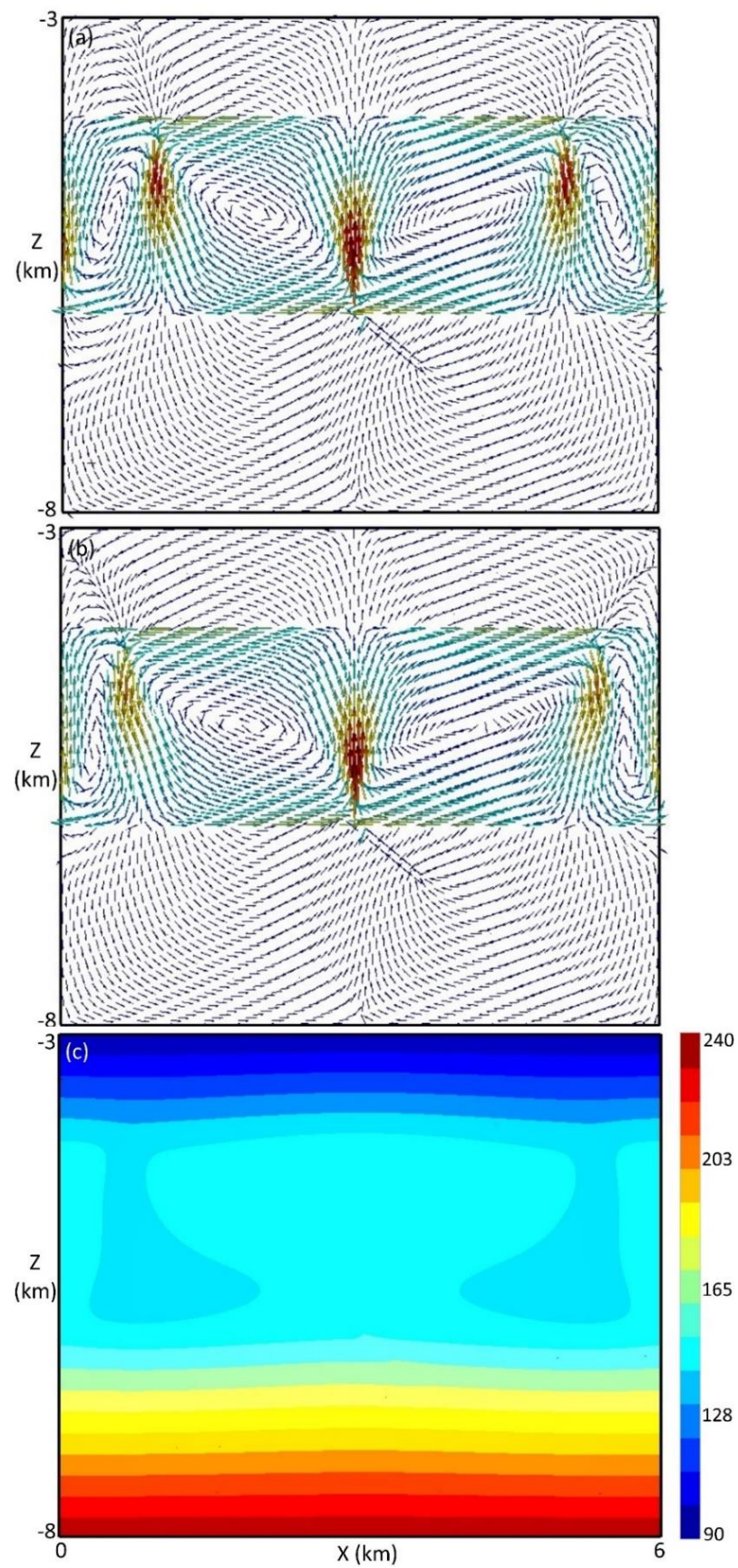
Figure 3. Numerical results for Scenario 1: (**a**) the flow vectors at 50,000 years, (**b**) the flow vectors at 300,000 years, and (**c**) the temperature distribution at 300,000 years.

The unconformity interface represents an oxidation-reduction front since it separates the sandstone layer in the oxidizing condition and the basement unit in the reducing condition. Therefore, at early time, a broad range of uraninite precipitation first occurs close to the unconformity when the oxidizing basinal fluid percolates into the basement and reacts with the reducing uranium-rich basement brine, according to Reaction (1). Figure 4a shows the precipitated uraninite at 10,000 years, which is characterized by a horizontal sheet-like shape immediately beneath the unconformity and has a max volume fraction of 2.52×10^{-7}. Uraninite mineralization also occurs along the cover–sandstone interface but with a much lower volume fraction. Accordingly, the concentration of UO_2^{2+} close to the unconformity in the basement is reduced due to its consumption for uranium precipitation. Thus, as time goes to late time, the basement brine becomes more important since it can drive deep aqueous uranium to shallow areas. As shown in Figure 3a, at 50,000 years, the basal brine is focused dominantly into the footwall area of the fault zone, which brings deep aqueous uranium up to react with the shallow oxidizing fluid that is percolated to the basement from the overlain sandstone and via the fault zone. Figure 4b illustrates the precipitated uraninite at 50,000 years. Now, more focused uranium precipitation occurs in the footwall with a higher volume fraction of 1.29×10^{-6}. Therefore, the footwall area in the basement seems to represent a favorable structural trap for uranium deposition. As time progresses, more basal brine is focused into the structural trap, refer to Figure 3b for instance, which brings more aqueous uranium from depth. This allows the uranium precipitation to grow up slowly with time in size and volume fraction. Figure 4c shows the precipitated uraninite at 150,000 years with a max volume fraction of 8.26×10^{-6}, and Figure 4d illustrates the precipitated uraninite at 300,000 years with a max volume fraction of 1.08×10^{-5}. The uranium deposit is located at the same structural trap, but as time increases from 150,000 to 300,000 years, the deposit becomes slightly greater in its size and volume fraction.
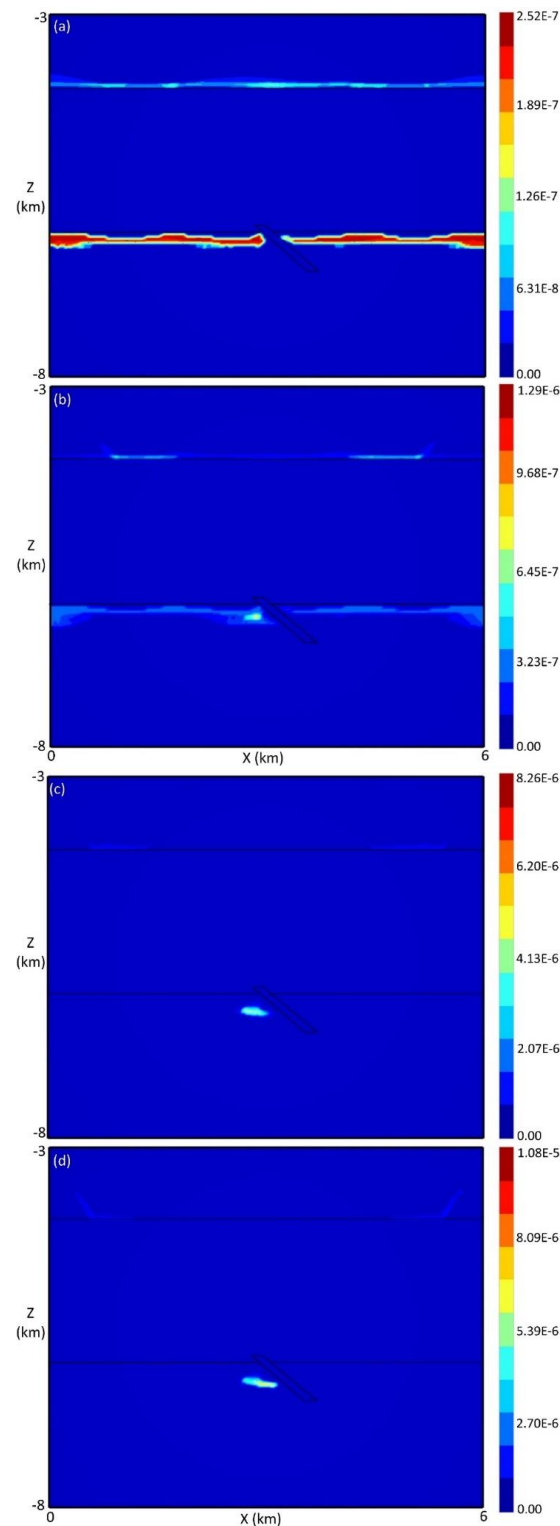
3.2. Scenario 2

Figure 5a shows the fluid flow vectors at 300,000 years when the fault zone moves upwards with an extension of 250 m above the unconformity and 375 m below it. Two dominant convection cells establish in the sandstone layer, with two minor cells close to the side boundaries. The fluid flow exhibits a similar pattern in comparison with that of Scenario 1 shown in Figure 3b. However, with more fault extension above the unconformity, the max flow rate now is 1.78 and 1.79×10^{-3} m/year, respectively, in the sandstone and basement unit, which is higher than that in Scenario 1. The temperature distribution in this case (not shown here) is also like that in Figure 3c. Figure 5b illustrates the precipitated uranium at 300,000 years, with a max volume fraction of 1.32×10^{-5}. Again, the uranium deposit is formed in the favorable structural trap, but with a greater volume fraction, which results likely from the higher flow rate in this scenario, compared with the above scenario.
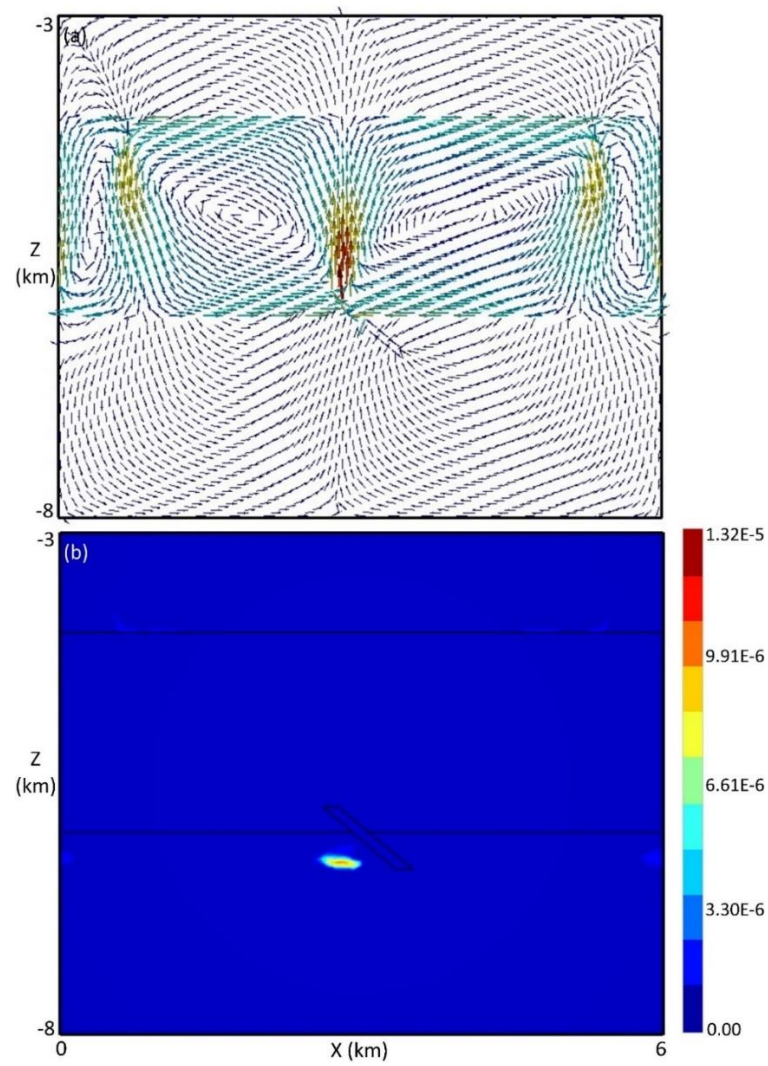
3.3. Scenario 3

Figure 6a shows the flow vectors at 300,000 years when the fault zone is mainly located in the sandstone layer. Now, one dominant convection cell and five narrow convection cells establish in the sandstone layer, which is different in comparison with the above two scenarios. The max flow rate is 1.54 and 1.71×10^{-3} m/year in the sandstone and basement, respectively. As shown in Figure 6b, the temperature distribution also differs significantly from that in Figure 3c. This is due to the convective heat transport by the two downwelling and two upwelling zones in the right half of the sandstone layer. More importantly, with limited extension of the fault zone below the unconformity, the basement brine in this scenario is not only focused into the footwall area, but also into other shallow areas in the basement beneath the upwelling flow zones in the overlain sandstone, as illustrated in Figure 6a. This is totally different from the above two scenarios, where almost all the basement brine is focused to the footwall area of the fault zone. Figure 6c shows the precipitated uraninite at 300,000 years. Now, main uraninite precipitation occurs in two

locations: one is in the footwall area under the central upwelling zone, and the other is close to the right side boundary. However, the max volume fraction is only 3.82×10^{-6}, substantially lower than those in other scenarios, which is clearly due to the less focusing of ore-forming fluids in the basement in this scenario. Weak uraninite precipitation also occurs in areas that are beneath the unconformity and spatially associated with other upwelling zones in the sandstone, but with even lower volume fraction, as illustrated in Figure 6c.
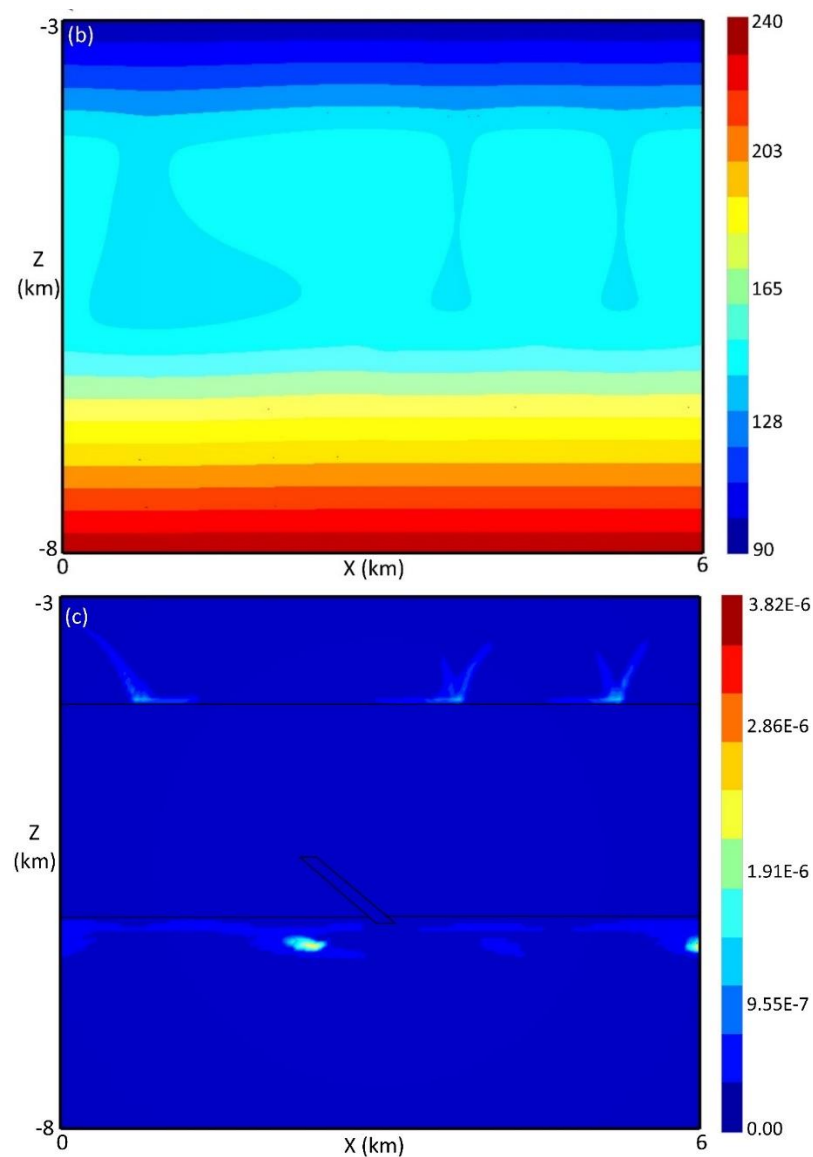

Figure 4. Numerical results of the precipitated uraninite and volume fraction for Scenario 1: (**a**) at 10,000 years, (**b**) at 50,000 years, (**c**) at 150,000 years, and (**d**) at 300,000 years.

Figure 5. Numerical results at 300,000 years for Scenario 2: (**a**) the flow vectors, and (**b**) the precipitated uraninite and volume fraction.
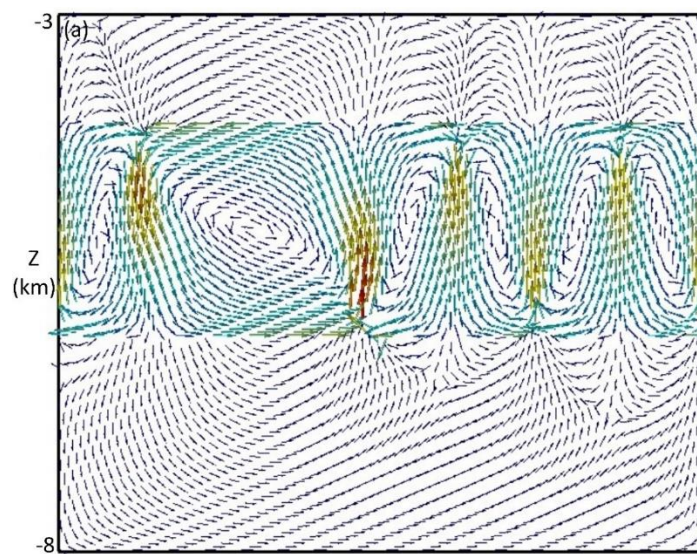
Figure 6. *Cont.*

Figure 6. Numerical results at 300,000 years for Scenario 3: (**a**) the flow vectors, (**b**) the temperature distribution, and (**c**) the precipitated uraninite and volume fraction.

4. Conclusions

Reactive flow modeling was conducted in this study to evaluate the role of fault extension relevant to the unconformity in controlling uranium ore genesis. Our numerical results indicate that the location of the faulted graphite zone determines the fluid flow pattern in both the sandstone layer and the basement unit, which in turn governs the transport of aqueous components, the uranium deposition, and the temperature distribution. For all the cases, at early time, uraninite precipitation initially occurs immediately beneath the unconformity, but with a very low volume fraction. At late time, however, different scenarios exhibit diverse behaviors. When the fault zone is located dominantly in the basement with a limited extension above the unconformity (Scenarios 1 and 2), almost all the reducing basement brine is focused into the footwall area of the fault zone, which reacts with the shallow oxidizing fluid that is percolated into the basement from the overlain sandstone layer via the downwelling zones and the fault. As a result, uranium deposits are formed in the footwall area beneath the unconformity. When the fault zone is mainly in the sandstone layer with a limited extension below the unconformity (Scenario 3), the focusing extent of ore-forming fluids is considerably lessened. Consequently, uranium precipitation occurs not only in the footwall but also in other areas below the upwelling flow zones in

the sandstone layer, all with a very low volume fraction. The footwall area of the fault zone in the basement is an ideal structural trap that is in favor of focusing fluids for uranium deposition, and therefore, it should be an exploration target in the field.

It should be noted that the numerical simulations we present in this paper are only two-dimensional. Full 3D reactive flow modeling is required in the near future in order to accurately simulate real-world ore-forming systems.

Author Contributions: Conceptualization, J.Y.; methodology, J.Y.; software, H.L. and X.X.; validation, X.X., H.L. and J.Y.; data collection and analysis, H.L., X.X. and J.Y.; writing—original draft preparation, H.L. and X.X.; writing—review and editing, J.Y.; visualization, H.L. and X.X.; funding acquisition, J.Y. All authors have read and agreed to the published version of the manuscript.

References

1. International Atomic Energy Agency. *Geological Classification of Uranium Deposits and Description of Selected Examples*; IAEA-TECDOC-1842; International Atomic Energy Agency: Vienna, Austria, 2018; ISBN 978-92-0-101618-8.
2. Cuney, M. The extreme diversity of uranium deposits. *Miner. Depos.* **2009**, *44*, 3–9. [CrossRef]
3. Dahlkamp, F.J. *Uranium Ore Deposits*; Springer: Berlin, Germany, 2013; pp. 1–15.
4. Fayek, M.; Kyser, T.K. Characterization of multiple fluid events and rare-earth-element mobility associated with formation of unconformity-type uranium deposits in the Athabasca Basin, Saskatchewan. *Can. Miner.* **1997**, *35*, 627–658.
5. Jefferson, C.W.; Thomas, D.J.; Gandhi, S.S.; Ramaekers, P.; Delaney, G.; Brisbin, D.; Cutts, C.; Quirt, D.; Portella, P.; Olson, R.A. Unconformity associated uranium deposits of the Athabasca Basin, Saskatchewan and Alberta. In *Mineral Deposits of Canada: A Synthesis of Major Deposit-Types, District Metallogeny, the Evolution of Geological Provinces, and Exploration Methods*; Goodfellow, W.D., Ed.; Special Publication; Geological Association of Canada, Mineral Deposits Division: Ottawa, ON, Canada, 2007; Volume 5, pp. 273–305.
6. Bruce, M.; Kreuzer, O.; Wilde, A.; Buckingham, A.; Butera, K.; Bierlein, F. Unconformity-type uranium systems: A comparative review and predictive modelling of critical genetic factors. *Minerals* **2020**, *10*, 738–793. [CrossRef]
7. Ramaekers, P.; Jefferson, C.W.; Yeo, G.M.; Collier, B.; Long, D.G.F.; Drever, G.; Mchardy, S.; Jiricka, D.; Cutts, C.; Wheatley, K.; et al. Revised geological map and stratigraphy of the Athabasca Group, Saskatchewan and Alberta. In: EXTECH IV: Geology and Uranium Exploration Technology of the Proterozoic Athabasca Basin, Saskatchewan and Alberta. *Geol. Surv. Can. Bull.* **2007**, *588*, 155–192.
8. Alexandre, P.; Kyser, K.; Thomas, D.; Polito, P.; Marlat, J. Geochronology of unconformity-related uranium deposits in the Athabasca Basin, Saskatchewan, Canada and their integration in the evolution of the basin. *Miner. Depos.* **2009**, *44*, 41–59. [CrossRef]
9. Hoeve, J.; Rawsthorn, K.; Quirt, D. Uranium metallogenetic studies: Clay mineral stratigraphy and diagenesis in the Athabasca Group. *Sask. Res. Counc. Publ.* **1981**, *22*, 76–89.
10. Halter, G. Zonality of Alterations in the Environment of Uranium Deposits Associated to Middle Proterozoic Unconformity (Saskatchewan, Canada). Ph.D. Thesis, Université Louis Pasteur, Strasbourg, France, 1988; 252p.
11. Kotzer, T.G.; Kyser, T.K. Petrogenesis of the Proterozoic Athabasca Basin, northern Saskatchewan, Canada, and its relation to diagenesis, hydrothermal uranium mineralization and paleohydrology. *Chem. Geol.* **1995**, *120*, 45–89. [CrossRef]
12. Renac, C.; Kyser, T.K.; Durocher, K.; Dreaver, G.; O'Connor, T. Comparison of diagenetic fluids in the Proterozoic Thelon and Athabasca Basins, Canada: Implications for protracted fluid histories in stable intracratonic basins. *Can. J. Earth Sci.* **2002**, *39*, 113–132. [CrossRef]
13. Derome, D.; Cathelineau, M.; Cuney, M.; Fabre, C.; Lhomme, T.; Banks, D.A. Mixing of sodic and calcic brines and uranium deposition at McArthur River, Saskatchewan, Canada: A Raman and laser-induced breakdown spectroscopic study of fluid inclusions. *Econ. Geol.* **2005**, *100*, 1529–1545. [CrossRef]
14. Hoeve, J.; Sibbald, T.I. On the genesis of Rabbit Lake and other unconformity-type uranium deposits in northern Saskatchewan, Canada. *Econ. Geol.* **1978**, *73*, 1450–1473. [CrossRef]
15. Kyser, T.K.; Wilson, M.R.; Ruhrmann, G. Stable isotope constraints on the role of graphite in the genesis of unconformity-type uranium deposits. *Can. J. Earth Sci.* **1989**, *26*, 490–498. [CrossRef]
16. Hoeve, J.; Quirt, D. Mineralization and host rock alteration in relation to clay mineral diagenesis and evolution of the middle-Proterozoic, Athabasca Basin, northern Saskatchewan, Canada. *Sask. Res. Counc. Tech. Rep.* **1984**, *187*, 187.

17. Pascal, M.; Ansdell, K.M.; Annesley, I.R. Graphite-bearing and graphite-depleted basement rocks in the Dufferin Lake zone, south-central Athabasca Basin, Saskatchewan. In *Targeted Geoscience Initiative 4: Unconformity-Related Uranium Systems*; Potter, E.G., Wright, D.M., Eds.; Geological Survey of Canada Open File; Natural Resources Canada: Ottawa, ON, Canada, 2015; Volume 7791, pp. 83–92.

18. Potter, E.G.; Wright, D.M. Targeted geoscience initiative 4: Unconformity-related uranium systems. In *Geological Survey of Canada Open File*; Natural Resources Canada: Ottawa, ON, Canada, 2015; Volume 7791, p. 126. [CrossRef]

19. Bruneton, P. Geological environment of the Cigar Lake uranium deposit. *Can. J. Earth Sci.* **1993**, *30*, 653–673. [CrossRef]

20. Hajnal, Z.; Györfi, I.; Annesley, I.R.; White, D.J.; Powell, B.; Koch, R. Seismic reflections outline complex structural setting of the uranium in the Athabasca Basin. In Uranium production and raw materials for the nuclear fuel cycle: Supply and demand, economics, the environment and energy security. Extended synopses, Report IAEA-CN-128. In Proceedings of the An International Symposium Held in Vienna, Vienna, Austria, 20–24 June 2005.

21. Finch, W. Uranium provinces of North America: Their definition, distribution, and models. *US Geol. Surv. Bull.* **1996**, *2141*, 1–15.

22. Bishop, C.; Mainville, A.; Yesnik, L. *Cigar Lake Operation Northern Saskatchewan, Canada*; Cameco Technical Report; National Instrument: Austin, TX, USA, 2016; pp. 1–164.

23. McGill, B.; Marlatt, J.; Matthews, R.; Sopuck, V.; Homeniuk, L.; Hubregtse, J. The P2 North uranium deposit Saskatchewan, Canada. *Explor. Min. Geol.* **1993**, *2*, 321–331.

24. Li, Z.; Chi, G.; Bethune, K. The effects of basement faults on thermal convection and implications for the formation of unconformity-related uranium deposits in the Athabasca Basin, Canada. *Geofluids* **2016**, *16*, 729–751. [CrossRef]

25. Eldursi, K.; Chi, G.; Bethune, K.; Li, Z.; Ledru, P.; Quirt, D. New insights from 2- and 3-D numerical modelling on fluid flow mechanisms and geological factors responsible for the formation of the world-class Cigar Lake uranium deposit, eastern Athabasca Basin, Canada. *Miner. Depos.* **2020**, *56*, 1365–1388. [CrossRef]

26. Caine, J.S.; Evans, J.P.; Forster, C.B. Fault zone architecture and permeability structure. *Geology* **1996**, *24*, 1025–1028. [CrossRef]

27. Cui, T.; Yang, J.; Samson, I.M. Tectonic deformation and fluid flow: Implications for the formation of unconformity-related uranium deposits. *Econ. Geol.* **2012**, *107*, 147–163. [CrossRef]

28. Cui, T.; Yang, J.; Samson, I.M. Solute transport across basement/cover interfaces by buoyancy-driven thermohaline convection: Implications for the formation of unconformity-related uranium deposits. *Am. J. Sci.* **2012**, *312*, 994–1027. [CrossRef]

29. Pek, A.A.; Malkovsky, V.I. Linked thermal convection of the basement and basinal fluids in formation of the unconformity-related uranium deposits in the Athabasca Basin, Saskatchewan, Canada. *Geofluids* **2016**, *16*, 925–940. [CrossRef]

30. Raffensperger, J.P.; Garven, G. The formation of unconformity-type uranium ore deposits 2. coupled hydrochemical modeling. *Am. J. Sci.* **1995**, *295*, 639–696. [CrossRef]

31. Aghbelagh, Y.B.; Yang, J. Effect of graphite zone in the formation of unconformity-related uranium deposits: Insights from reactive mass transport modeling. *J. Geochem. Explor.* **2014**, *144*, 12–27. [CrossRef]

32. Aghbelagh, Y.B.; Yang, J. Role of hydrodynamic factors in controlling the formation and location of unconformity-related uranium deposits: Insights from reactive-flow modeling. *Hydrogeol. J.* **2017**, *25*, 465–486. [CrossRef]

33. Bear, J. *Dynamics of Fluids in Porous Media*; American Elsevier Publishing Company: Princeton, NJ, USA, 1972; p. 764.

34. Xu, T.; Spycher, N.; Sonnenthal, E.; Zhang, G.; Zheng, L.; Pruess, K. TOUGHREACT Version 2.0: A simulator for subsurface reactive transport under non-isothermal multiphase flow conditions. *Comput. Geosci.* **2011**, *37*, 763–774. [CrossRef]

35. Richard, A.; Rozsypal, C.; Mercadier, J.; Cuney, M.; Boiron, M.C.; Cathelineau, M.; Banks, D.A. Giant uranium deposits formed from exceptionally uranium-rich acidic brines. *Nat. Geosci.* **2012**, *5*, 142–146. [CrossRef]

36. Richard, A.; Cathelineau, M.; Boiron, M.C.; Mercadier, J.; Banks, D.A.; Cuney, M. Metal-rich fluid inclusions provide new insights into unconformity-related U deposits (Athabasca Basin and Basement, Canada). *Miner. Depos.* **2016**, *51*, 249–270. [CrossRef]

37. Chi, G.; Chu, H.; Petts, D.; Potter, E.; Jackson, S.; Williams-Jones, A. Uranium-rich diagenetic fluids provide the key to unconformity-related uranium mineralization in the Athabasca Basin. *Sci. Rep.* **2019**, *9*, 5530. [CrossRef]